Power Electronics and Drives
Volume 11(46), 2026 DOI: 10.2478/pead-2026-0032

Performance Analysis of PMSM Servo-drive with Model Predictive Control Schemes for Moment of Inertia Variations

Research paper

Hubert Lisiński*, Tomasz Tarczewski

Institute of Engineering and Technology, Faculty of Physics, Astronomy and Informatics, Nicolaus Copernicus University in Toruń, ul. Grudziądzka 5, 87-100 Toruń, Poland.

Received: 01 July, 2026; Received in the revised form: 06 September, 2026; Accepted: 06 October 2026

Abstract: With the continuous development of robotics, specifically regarding walking robots and advanced manipulators, alongside the accelerating electrification of manufacturing plants, the diversity of applications and environments in which servo-drives must operate is expanding significantly. Consequently, this increases the requirements for accurate trajectory tracking and robustness to parameter variations, while maintaining high efficiency characterised by low current and speed ripples. To address these challenges, this paper proposes predictive control solutions for Permanent Magnet Synchronous Motor (PMSM) servo-drives that ensure high-precision position control and robustness to variations in the moment of inertia, and compares their performance with that of the classical cascaded control structure (CCS). The authors implement both a novel full and a hybrid scheme of the fast gradient method model predictive position control (FGM-MPPC) and introduce a novel predictive current control scheme, termed preliminary voltage vector selecting model predictive current control (PVVS-MPCC), which generates candidate voltage vectors via a non-linear function. The investigations were conducted using a variable-frequency sinusoidal reference trajectory under three distinct system inertia values. The research results demonstrate that the application of a hybrid CCS utilising PVVS-MPCC effectively reduces current and speed ripples while enhancing system robustness. Conversely, the implementation of the full FGM-MPPC provides greater robustness and improved trajectory-tracking accuracy at low speeds.

Keywords: *servo-drive • permanent magnet synchronous motor • model predictive control • robustness analysis • variable frequency sinusoidal reference signal*

1. Introduction

PMSM servo-drives are widely used in applications requiring precise motion control, including numerically controlled machine tools, industrial and legged robots, unmanned aerial vehicles and aerospace systems (Bahari et al., 2026; Liu et al., 2026; Rinaldini et al., 2025; Sun et al., 2025). They are also employed in auxiliary actuation systems, such as aircraft ailerons and satellite mechanisms (Zuo et al., 2024). These applications impose demanding, often conflicting control requirements, since the servo-drive must maintain high positioning accuracy over a wide range of velocities and accelerations while remaining robust to variations in operating conditions and mechanical parameters, and ensuring low ripple in speed and current. Maintaining consistent performance across the entire operating frequency range is challenging. Therefore, selecting an appropriate control strategy for the servo-drive is essential to balancing precision, dynamic performance and robustness.

The most common position-control topology in industrial drives is the cascaded control structure (CCS). The widespread use of the CCS results primarily from its simple architecture, the straightforward enforcement of limits on internal variables, and the ease of tuning its proportional-integral (PI) controllers. However, PI controllers are increasingly combined with more advanced control methods to form hybrid structures. This trend is mainly driven

*Email: hubert.lisinski@umk.pl

Open Access. © 2026 Authors, published by Wroclaw University of Science and Technology. This is an open access article licensed under the Creative Commons Attribution License (http://creativecommons.org/licenses/by/4.0/).

by limitations of conventional PI control in systems requiring fast dynamic responses or involving non-linear plant behaviour. In particular, PI controllers are frequently combined with model predictive control (MPC), which can explicitly account for non-linearities and complex multivariable constraints while improving system dynamic response (Bolun et al., 2022; Xu et al., 2025; Zheng et al., 2023; Zuo et al., 2024). In Xu et al. (2025), a deadbeat-based MPC approach was applied, whereas (Zuo et al., 2024) employed finite control set MPC (FCS-MPC). In both methods, MPC was implemented as the current controller, resulting in an improved dynamic response of the controlled system. Predictive mechanical variable control has been investigated in Bolun et al. (2022) and Zheng et al. (2023). In the former approach, the optimal control action was derived using an incremental PMSM model by setting the partial derivative of the cost function to zero. In the latter, explicit MPC (EMPC) was employed, with the quadratic optimisation problem solved offline. The online computation was therefore limited to identifying the appropriate region corresponding to the optimal output. Fully model predictive position control (MPPC) has received considerably less attention in the literature than hybrid control structures (He et al., 2024; Li et al., 2026; Wang et al., 2025; Zhang et al., 2026). An FCS-MPC position controller was proposed in Zhang et al. (2026), demonstrating improved tracking of an S-shaped position reference and robustness to variations in motor resistance and inductance. However, the influence of variations in the moment of inertia was not considered. In He et al. (2024), the position MPC is based on Laguerre functions, which provided higher positioning accuracy for step and sinusoidal reference signals at 5 Hz and 10 Hz, but no comprehensive analysis of a variable-frequency sinusoidal reference signal was performed. A fully predictive position controller based on an incremental model was presented in Wang et al. (2025), while Li et al. (2026) proposed an offset-free MPC based on a Kalman filter. Both studies focused mainly on constraint handling and methods for maintaining drive performance when the constraints became active. To sum up, the existing studies provide only limited information on controller-tuning procedures, a comprehensive variable-frequency sinusoidal reference signal and robustness to variations in the moment of inertia.

This paper introduces a full and a hybrid scheme of the fast gradient method model predictive position control (FGM-MPPC), which, to the best of the authors' knowledge, has not previously been investigated for servo-drive systems, and utilises an original predictive current control scheme, termed preliminary voltage vector selecting model predictive current control (PVVS-MPCC), which generates candidate voltage vectors via a non-linear function. Next, it compares four position control approaches: full CCS, hybrid CCS with PVVS-MPCC, FGM-MPPC and a hybrid FGM-MPPC with a PI current controller. The hybrid CCS utilising the PVVS-MPCC method is based on an original approach to candidate voltage generation that relies on designing a non-linear function derived from the error between the predicted and reference current vectors. Each method was evaluated using time-domain response analysis with a sinusoidal excitation signal and varying acceleration for three different inertia values, an assessment that, to the best of the authors' knowledge, has not previously been conducted for PMSM servo-drives employing predictive control structures. The cascaded CCS and hybrid CCS using PVVS-MPCC controllers were tuned using pole placement and internal model control (IMC) (Bożek and Trybus, 2022; Brandstetter and Krecek, 2012), whereas the FGM-MPPC methods were tuned using the Artificial Bee Colony (ABC) optimisation algorithm (Tarczewski and Grzesiak, 2018).

The motivation for investigating the tracking performance of CCS, PVVS-MPCC, FGM-MPPC and hybrid FGM-MPPC under a variable-frequency sinusoidal reference trajectory stems from the lack of studies providing a comprehensive comparison of full and hybrid predictive control structures across different configurations. Such an investigation allows for a clear assessment of differences in tracking accuracy, ripple of key state variables and robustness to variations in the moment of inertia, as these characteristics are rarely evaluated together in the literature (He et al., 2024; Li et al., 2026; Wang et al., 2025; Zhang et al., 2026). Furthermore, the proposed PVVS-MPCC approach is motivated by the growing interest in hybrid control methods combining FCS-MPC and CCS-MPC. Existing approaches may be sensitive to model inaccuracies and variations in the reference current generated by the outer control loop, or may require additional tuning. This motivates the development of alternative solutions, such as the proposed preliminary voltage-vector selection based on a non-linear function, which offers an approach distinct from conventional low-pass filtering or deadbeat methods.

This paper is divided into five sections. In Section 2, the authors present both the continuous-time and discretised models of the PMSM. Section 3 provides a detailed description of the investigated control structures, while Section 4 describes the experimental test bench and presents the experimental results along with their comprehensive analysis. Section 5 summarises the conclusions drawn from the conducted experiments and outlines potential directions for future research.

2. Model of PMSM servo-drive

Developing a high-performance position controller requires thorough knowledge of the actuator system. This is crucial for implementing MPC, feedforward components, load torque observer, and tuning PI regulators in CCS via analytical methods. The investigations in this paper were conducted on a Surface Permanent Magnet Synchronous Motor (SPMSM). This specific motor type is characterised by symmetrically distributed stator inductances in the *dq* axes, meaning that $L_d = L_q = L_s$. Consequently, this yields a simplified motor model, whose state-space representation is provided below:

$$\frac{dx(t)}{dt} = Ax(t) + Bu(t) + Ed(t) \tag{1}$$

with:

$$x(t) = \begin{bmatrix} i_d(t) \\ i_q(t) \\ \omega(t) \\ \theta(t) \end{bmatrix}, u(t) = \begin{bmatrix} u_d(t) \\ u_q(t) \end{bmatrix}, d(t) = \hat{T}_L(t), A = \begin{bmatrix} -\frac{R_s}{L_s} & p\omega(t) & 0 & 0 \\ -p\omega(t) & -\frac{R_s}{L_s} & \frac{p\psi_f}{L_s} & 0 \\ 0 & \frac{K_t}{J_m} & -\frac{B_m}{J_m} & 0 \\ 0 & 0 & 0 & 1 \end{bmatrix}, B = \begin{bmatrix} \frac{K_p}{L_s} & 0 \\ 0 & \frac{K_p}{L_s} \\ 0 & 0 \\ 0 & 0 \end{bmatrix}, E = \begin{bmatrix} 0 \\ 0 \\ -\frac{1}{J_m} \\ 0 \end{bmatrix}$$

where: $i_d(t)$, $i_q(t)$ – measured currents, $\omega(t)$ – measured speed, $\theta(t)$ – measured rotor position, $u_d(t)$, $u_q(t)$ – voltage vector components, K_p – gain of voltage source inverter (VSI), R_s, L_s – stator resistance and inductance, ψ_f – flux from permanent magnets, p – number of pole pairs, B_m – viscous friction, J_m – moment of inertia and $T_L(t)$ – load torque. For the considered PMSM, the electromagnetic torque is defined as:

$$T_e(t) = \frac{3}{2} p\psi_f i_q(t) = K_t i_q(t) \tag{2}$$

where: K_t – torque constant. From Eq. (2), it can be seen that the identical inductance values also simplify the torque equation, and the electromagnetic torque is directly influenced solely by the $i_q(t)$ current component. To implement predictive control methods and the load torque observer, a discrete-time model representation is essential. This discrete model was obtained using the forward Euler approximation method, and its formulation is presented below:

$$x(k+1) = A_d x(k) + B_d u(k) + E_d d(k) \tag{3}$$

with:

$$x(k) = \begin{bmatrix} i_d(k) \\ i_q(k) \\ \omega(k) \\ \theta(k) \end{bmatrix}, u(k) = \begin{bmatrix} u_d(k) \\ u_q(k) \end{bmatrix}, d(k) = \hat{T}_L(k),$$

$$A_d = \begin{bmatrix} 1 - T_s\frac{R_s}{L_s} & pT_s\omega(k) & 0 & 0 \\ -pT_s\omega(k) & 1 - T_s\frac{R_s}{L_s} & -T_s\frac{p\psi_f}{L_s} & 0 \\ 0 & T_s\frac{K_t}{J_m} & 1 - T_s\frac{B_m}{J_m} & 0 \\ 0 & 0 & T_s & 1 \end{bmatrix}, B_d = \begin{bmatrix} T_s\frac{K_p}{L_s} & 0 \\ 0 & T_s\frac{K_p}{L_s} \\ 0 & 0 \\ 0 & 0 \end{bmatrix}, E_d = \begin{bmatrix} 0 \\ 0 \\ -\frac{T_s}{J_m} \\ 0 \end{bmatrix}$$

where: T_s – sampling time, k – number of the discrete-time sample.

3. Position Control Structure

3.1. Cascaded control structure

The classical cascaded position control structure consists of three PI controllers connected in series, along with feedforward paths that improve tracking performance for complex reference trajectories, such as S-curve profiles. The schematic diagram of the CCS implemented in the experimental drive system is presented in Figure 1(a). Manual tuning of the CCS is relatively simple, which constitutes one of its main advantages. However, such an approach does not guarantee optimal control performance. Therefore, in this study, the IMC method (Brandstetter and Krecek, 2012) was used to tune the current controller, while the pole-placement approach proposed in Bożek and Trybus (2022) was applied to the speed and position controllers. To improve the control performance, the feedforward gains $K_{f\omega}$, K_{fa} were determined based on the inverse mathematical model of the motor (Mandra, 2014). Cascaded control using PI controllers is generally designed based on a linearised model, whereas the electrical model of PMSM exhibits cross-coupling between the *d* and *q* axes. Therefore, a linearisation mechanism is required. In this study, decoupling-based linearisation was applied as described in Tarczewski et al. (2018).

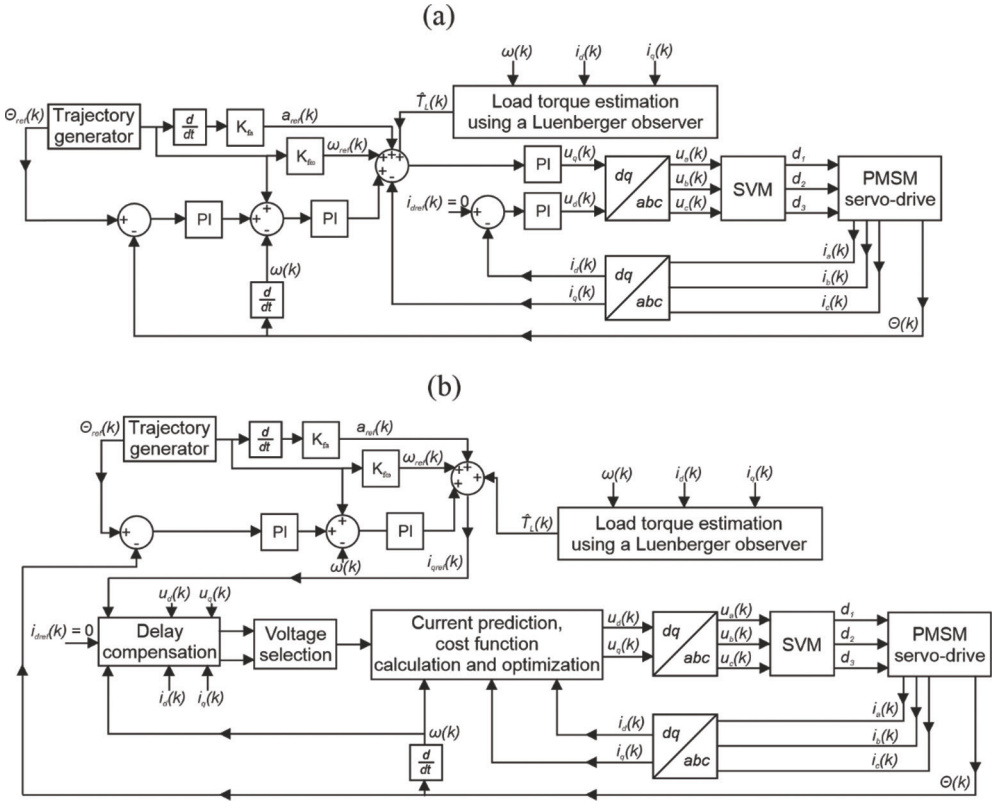


Figure 1. Block diagram of (a) classical and (b) hybrid cascaded servo-drive control structures. PI, proportional-integral.

Replacing the PI current controller with a predictive one yields a hybrid control structure that improves current dynamics. MPCC has been reported in the literature (Kawai et al., 2023; Sun et al., 2025). In this paper, however, the authors propose the original PVVS-MPCC method. The proposed hybrid control structure is presented in Figure 1(b). In predictive control systems, compensation of computational and measurement delays is commonly used due to the relatively high computational complexity of the algorithm (Zhuang et al., 2022). For this purpose, an initial prediction step is performed before the main iterative loop using Eq. (2). The predicted current values obtained in this stage are subsequently utilised within the main optimisation loop as follows:

$$i_d(k+2) = T_s \frac{K_p}{L_s} u_d(k) + \left(1 - T_s \frac{R_s}{L_s}\right) i_d(k+1) + pT_s \omega(k) i_q(k+1) \tag{4}$$

$$i_q(k+2) = T_s \frac{K_p}{L_s} u_q(k) + \left(1 - T_s \frac{R_s}{L_s}\right) i_q(k+1) - pT_s \omega(k) i_d(k+1) - T_s \frac{p\psi_f}{L_s} \omega(k) \tag{5}$$

The PVVS-MPCC method defines these candidates via a non-linear function of the tracking error, which is computed as the difference between the predicted current $i_q(k + 1)$ and $i_d(k + 1)$ and their corresponding reference values. Subsequently, the output value of this function is projected onto each quadrant of the *dq* coordinate system. This projection yields four symmetrical candidate voltage vectors within the *dq* space:

$$V_{i,j}(k) = \begin{bmatrix} u_d^{i,j}(k) \\ u_q^{i,j}(k) \end{bmatrix} \tag{6}$$

$$K_p u_d^{i,j}(k) = (-1)^i g\left(e_d(k)\right) \tag{7}$$

$$K_p u_q^{i,j}(k) = (-1)^j g\left(e_q(k)\right) \tag{8}$$

with:

$$e_d(k) = i_{dref}(k) - i_d(k+2) \tag{9}$$

$$e_q(k) = i_{qref}(k) - i_q(k+2) \tag{10}$$

where: i, j = {0, 1}. The introduction of the non-linear function $g(e)$ enables the control response to adapt to the drive system's actual operating conditions. The objective is to reduce the sensitivity of the function to disturbances; therefore, for small values of e, the value of $g(e)$ should remain close to zero, while for the maximum possible current change, it should reach a value as close as possible to its maximum. Such behaviour is characteristic of power functions. A natural choice would be a quadratic function; however, due to the cogging torque in the PMSM, a wider flat region was desirable. Increasing the polynomial order allows a greater flattening of the function for small values of x. Based on experimental evaluation, the best results were obtained using the following form of the $g(e)$ function:

$$g(e) = \alpha e^4 - \beta e^3 + \gamma e^2 \tag{11}$$

with the coefficients: α, β, γ defined in the latter part of this paper. The voltages calculated from Eqs (7) and (8), incorporating the non-linear function Eq. (11), are fed into the optimisation loop. Such a candidate voltage vector definition strategy for the optimisation loop is expected to ensure low current and speed ripple under slowly varying reference position conditions, since the non-linear function limits the voltage magnitude for small variations of the reference current. Conversely, for rapidly varying reference positions and corresponding changes in the reference current, the available voltage vectors are significantly amplified, thereby enabling fast error compensation and improved dynamic response. The calculated voltage components for large differences, according to Eqs (9) and (10), may exceed the maximum voltage the inverter can supply. Therefore, the resulting voltage vectors are constrained to a circle of radius K_p. In the optimisation loop, system-state predictions are performed for each candidate voltage using Eq. (2), and the corresponding cost function value is evaluated. This cost function serves as the selection criterion for the optimal control voltage vector. The cost function formulated in this paper is presented below:

$$J_{\text{PVVS}} = i_d(k+2)^2 + \left(i_{qref} - i_q(k+2)\right)^2 \tag{12}$$

The i_{qref} is generated by the outer cascaded PI controllers, whereas the i_{dref} is set to zero. This approach stems from the fact that the i_d current does not influence the electromagnetic torque Eq. (3). Constraints in the cascaded control topology are managed by hard-limiting the reference values, independent of the specific architecture of the individual state-variable controllers. The structure of the proposed PVVS-MPCC method is illustrated in the block diagram in Figure 1(b). The voltage vector selected based on the cost function Eq. (12) is transformed into the *abc* reference frame and subsequently processed by Space Vector Modulation (SVM). The SVM decomposes the reference voltage vector into three vectors, two active vectors and one zero vector, and determines the corresponding application times for each vector and the duration d of the pulse width modulation (PWM) signal.

The PI controller tuning was initially performed using analytical methods (Bożek and Trybus, 2022; Brandstetter and Krecek, 2012). However, since the primary objective was to achieve the best possible trajectory tracking, the position controller's proportional gain was manually increased for both the full CCS and hybrid CCS methods until the measurement-noise amplification threshold was reached. The controller gains for the used control structures are presented in Table 1.

Table 1. PI controller gains for the proposed CCS.

Parameter	K_{pi}	K_{ii}	$K_{p\omega}$	$K_{i\omega}$	$K_{p\theta}$	$K_{i\theta}$
Full CCS	0.2386	82.6772	1.1800	8.3333	150	8.3333
Hybrid CCS	-	-	1.1800	8.3333	200	8.3333

CCS, cascaded control structure; PI, proportional-integral.

3.2. MPC with fast gradient method optimisation

Optimising the cost function involves minimising it, meaning the objective is to determine a set of input voltages $u(k + 1)$ that yields the lowest possible cost. In the gradient descent-based approach, the voltage increment in successive optimisation iterations is determined based on the gradient of the cost function, which can be formulated as follows:

$$y(n+1)=y(n)-\frac{1}{L}\nabla J\left(y(n)\right)=y(n)-\frac{1}{L}\frac{dJ\left(y(n)\right)}{dy} \tag{13}$$

$$y_u(n+1)=\begin{bmatrix}u_d(n+1)\\ u_q(n+1)\end{bmatrix}=\begin{bmatrix}u_d(n)-\frac{1}{L_f}\frac{dJ_f\left(u_d(n)\right)}{du_d}\\ u_q(n)-\frac{1}{L_f}\frac{dJ_f\left(u_q(n)\right)}{du_q}\end{bmatrix} \tag{14}$$

$$y_{iq}(n+1)=i_{qref}(n+1)=i_{qref}(n)-\frac{1}{L_h}\frac{dJ_h\left(i_{qref}(n)\right)}{di_{qref}} \tag{15}$$

where: L – Lipschitz constant, L_f – Lipschitz constant for full FGM-MPPC, L_h – Lipschitz constant for hybrid FGM-MPPC, n – number of iteration. Eqs (14) and (15) provide a detailed formulation for the two cases considered in this paper: full FGM-MPPC Eq. (14) and hybrid FGM-MPPC coupled with a PI current controller Eq. (15). The cost function can take various forms depending on the control objectives, available system information and the supply system topology (Karamanakos et al., 2020). In this study, the following cost functions were implemented:

$$J_f\left(y_u(n)\right)=W_d i_d(k+2)^2+W_q\left(i_q(k+2)-i_{qref}{}^f\right)^2+W_\omega\left(\omega(k+2)-\omega_{ref}\right)^2+W_\theta\left(\theta(k+2)-\theta_{ref}\right)^2+W_u y_u(n)^2 \tag{16}$$

$$J_h\left(y_{iq}(n)\right)=W_\omega\left(\omega(k+2)-\omega_{ref}\right)^2+W_\theta\left(\theta(k+2)-\theta_{ref}\right)^2+W_{iq}y_{iq}(n)^2 \tag{17}$$

where: W_q, W_d, W_ω, W_θ – weighting factors associated with the prediction terms of i_d, i_q, ω, θ, W_{iq} – weighting factor for i_{qref} terms, which is the objective in the hybrid FGM-MPPC, W_u – weighting factors associated with the voltage components u_q, u_d, which constitute the objective in the full FGM-MPPC. Eq. (16) corresponds to the full FGM-MPPC, whereas Eq. (17) represents the hybrid predictive control scheme integrated with a PI current controller. The reference values ω_{ref} and θ_{ref} are generated by a trajectory planning algorithm. While the i_{qref} current in the hybrid FGM-MPPC configuration is derived from the gradient optimisation, for the full MPC scheme, it was determined analytically based on the differential equation of the mechanical subsystem, and is formulated as follows:

$$i_{qref}{}^f=\frac{B_m\omega_{ref}(k)}{K_t}+\frac{\hat{T}_L(k)}{K_t}+\frac{J_m}{K_t}\frac{\omega_{ref}(k)-\omega_{ref}(k-1)}{T_s} \tag{18}$$

where: $\hat{T}_L(k)$ – estimated load torque from Luenberger observer. The partial derivatives of the cost functions (16) and (17) are formulated as follows:

$$\frac{dJ_f\left(u_d(n)\right)}{du_d} = 2W_d\frac{T_s}{L_s}i_d(k+2) + 2W_u u_d(n) \tag{19}$$

$$\frac{dJ_f\left(u_q(n)\right)}{du_q} = 2W_q\frac{T_s}{L_s}(i_q(k+2) - i_{qref}{}^f) + 2W_\omega\frac{T_s^2K_t}{J_mL_s}\left(\omega(k+2)-\omega_{ref}\right) + 2W_\theta\frac{T_s^3K_t}{J_mL_s}\left(\theta(k+2)-\theta_{ref}\right) + 2W_u u_q(n) \tag{20}$$

$$\frac{dJ_h\left(i_{qref}(n)\right)}{di_{qref}} = 2W_\omega\frac{T_sK_t}{J_m}\left(\omega(k+2)-\omega_{ref}\right) + 2W_\theta\frac{T_s^2K_t}{J_m}\left(\theta(k+2)-\theta_{ref}\right) + 2W_{iq}i_{qref}(n) \tag{21}$$

The Lipschitz constant is a parameter interpreted as the optimisation step size. This parameter is critical for optimisation convergence and strictly depends on the rate of change of the gradient. Therefore, the Lipschitz constant L must satisfy the following condition:

$$\|\nabla J\left(y(n+1)\right) - \nabla J\left(y(n)\right)\| \le L\,\|\,y(n+1) - y(n)\| \tag{22}$$

$$L = \lambda_{max}(H) \tag{23}$$

Determining the largest eigenvalue of the Hessian matrix H Eq. (23) allows for finding the minimum value of L that satisfies condition Eq. (22), which is equivalent to establishing the maximum possible optimisation step size. This paper considers two distinct cost functions, J_f and J_h, which differ both in their number of constituent components and in the interpretation of their control outputs. The different cost-function formulations used by the methods yield distinct final definitions of the Lipschitz constants. The equations defining the constants L_f and L_h:

$$L_f = 2W_q\left(\frac{T_s}{L_s}\right)^2 + 2W_\omega\left(\frac{T_s^2K_t}{J_mL_s}\right)^2 + 2W_\theta\left(\frac{T_s^3K_t}{J_mL_s}\right)^2 + 2W_u \tag{24}$$

$$L_h = 2W_\omega\left(\frac{T_sK_t}{J_m}\right)^2 + 2W_\theta\left(\frac{T_s^2K_t}{J_m}\right)^2 + 2W_{iq} \tag{25}$$

While determining the Lipschitz constant L_h was straightforward because the system had only a single output, computing L_f requires considering the 2 × 2 Hessian matrix H. In practice, however, the cross-couplings have a negligible impact on the steepness of the cost function, as does the d-axis voltage u_d. Therefore, the solution can be simplified by defining L_f as the second derivative of the cost function with respect to u_q.

The Fast Gradient Method is an iterative algorithm that repeatedly solves Eq. (13), for $n = \{0, 1, \ldots, N\}$, where N denotes the maximum number of iterations, determined by the cost function's convergence rate. An insufficient number of iterations can severely degrade control quality, whereas an excessively high value unnecessarily increases the algorithm's computational complexity without yielding significant performance gains. Therefore, the number of iterations was empirically determined to be $N = 5$. The initial conditions $y(0)$ are reset to the currently measured values each time the algorithm is invoked. Specifically, $y_u(0) = [u_d(k),\ u_q(k)]'$ and $iqref(0) = iq(k)$. Although Eq. (13) allows the quadratic programming problem to be solved using the standard gradient descent method, many iterations are required to obtain an accurate solution. To overcome this limitation, Nesterov's accelerated gradient algorithm is applied in practice (Richter et al., 2010, 2012). This acceleration technique is based on computing the intermediate state variable $y(n + 1)$ using the following formulation:

$$y(n+1) = y(n) - \frac{1}{L}\nabla J\left(y(n)\right) + \delta\left(y(n) - \frac{1}{L}\nabla J\left(y(n)\right) - y(n-1) + \frac{1}{L}\nabla J\left(y(n-1)\right)\right) \tag{26}$$

where: δ – Nesterov momentum parameter. The structure of the FGM-MPC optimization loop is illustrated in Figure 2.

The cost functions (16) and (17) include weighting factors that require appropriate tuning. Favourable results can be achieved by utilising nature-inspired optimisation algorithms, such as particle swarm optimisation (PSO), pattern search (PS), or the ABC algorithm. In this study, the ABC method was employed, with its detailed implementation

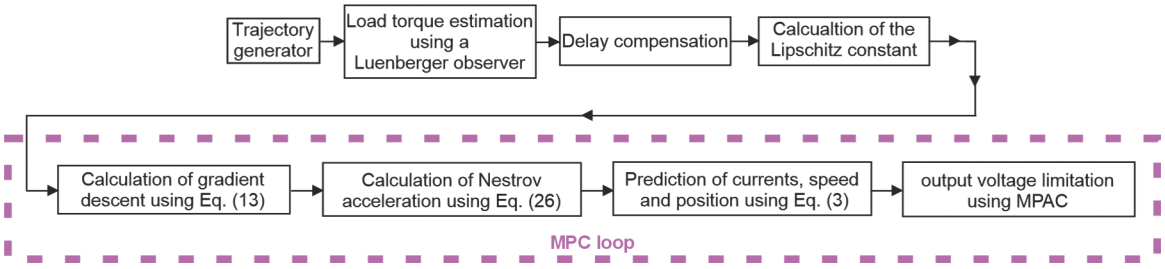


Figure 2. Block diagram of FGM-MPC control scheme. FGM-MPC, fast gradient method model predictive position control; MPAC, model predictive position control; MPC, model predictive control.

guidelines provided in Tarczewski and Grzesiak (2018). The cost function optimised by the metaheuristic algorithm is presented below:

$$J_{\mathrm{ABC}} = \sum_{m=0}^{M} T_s\left(\theta_{ref}(m) - \theta(m)\right) + \alpha T_s (i_{dref}(m) - i_d(m))^2 + \beta T_s (i_{qref}(m) - i_q(m))^2 \tag{27}$$

The values of the key parameters for the ABC tuning algorithm are presented in Table 2. The constraint values for W_ω and W_θ differ between the two methods because the hybrid FGM-MPPC approach exhibited severe oscillations when these values were too large, preventing the algorithm from finding optimal parameter settings. The weighting factor values obtained through this tuning method are summarised in Table 3. To enforce the motor state-variable constraints, the MPAC method was implemented (Tarczewski and Grzesiak, 2016).

Table 2. Parameters of autotuning algorithms.

Parameter	Full *FGM-MPPC*	Hybrid *FGM-MPPC*
No of colony size	10	10
No of food sources	5	5
Maximum no of cycles	40	40
Modification rate control parameter	0.8	0.8
Lower and upper bounds of W_q	$1 \cdot 10^{-3}$; $1 \cdot 10^{5}$	-
Lower and upper bounds of W_d	$1 \cdot 10^{-3}$; $1 \cdot 10^{5}$	-
Lower and upper bounds of W_ω	$1 \cdot 10^{-3}$; $1 \cdot 10^{5}$	$1 \cdot 10^{-3}$; $1 \cdot 10^{2}$
Lower and upper bounds of W_u	$1 \cdot 10^{-8}$; $1 \cdot 10^{1}$	$1 \cdot 10^{-3}$; $1 \cdot 10^{1}$
Lower and upper bounds of W_θ	$1 \cdot 10^{4}$; $1 \cdot 10^{13}$	$1 \cdot 10^{4}$; $1 \cdot 10^{8}$
Weighting coefficient of i_d error	0.001	0.001
Weighting coefficient of i_q error	0.0001	0.0001

FGM-MPPC, fast gradient method model predictive position control.

Table 3. Weighting factors of proposed FGM-MPC structures.

Parameter	W_q	W_d	W_ω	W_θ	W_u	W_{iq}
Full FGM-MPPC	910.3603	540.3114	$9.5353 \cdot 10^{4}$	10^{12}	0.5177	-
Hybrid FGM-MPPC	-	-	1.0046	$8.8582 \cdot 10^{7}$	-	0.0333

FGM-MPPC, fast gradient method model predictive position control.

4. Experimental Results

4.1. Laboratory setup and study methodology

The proposed control schemes were experimentally validated on a prototype PMSM servo drive. Figure 3 illustrates the general block diagram and photo of the laboratory setup featuring two PMSM drives. The load drive was controlled by a commercial VSI through a Kollmorgen AKD drive. The main system utilises a prototype VSI with *SiC* power

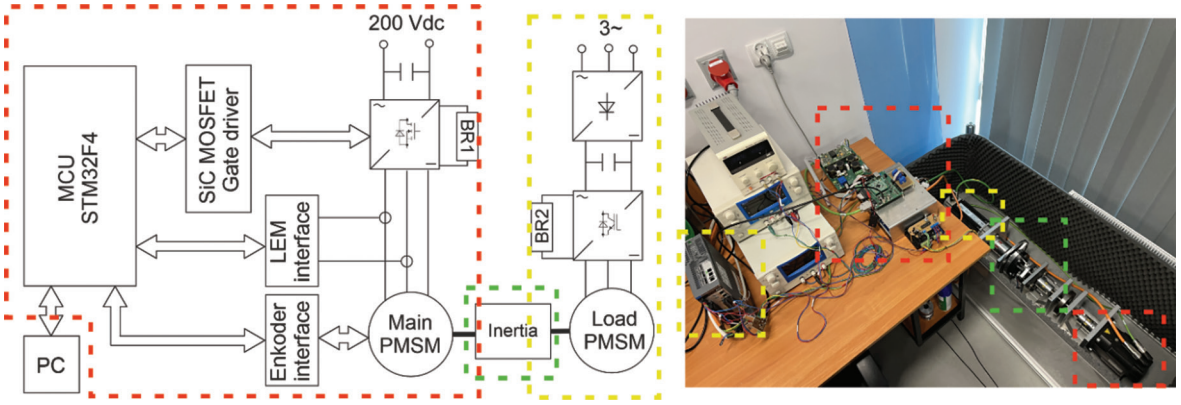


Figure 3. Laboratory setup.

devices to supply the tested motor. The control algorithms and peripheral software components were implemented on an STMicroelectronics ARM Cortex-M4 microcontroller. The control loop was executed at a sampling frequency of 10 kHz. The angular position of the motor shaft is obtained from a single-turn absolute encoder, Sick Stegmann SRS 50, with a resolution of 15 bits, corresponding to ca. $2 \cdot 10^{-4}$ rad. Both motors are connected via a clutch and a mechatronic system that allows changes in moment of inertia. The primary parameters of the investigated drive are summarised in Table 4.

Table 4. Parameters of the servo-drive.

Parameter	Symbol & unit	Value
Rated power	P_N [kW]	1.73
Flux of a permanent magnet	ψ_f [Wb]	$25.44 \cdot 10^{-2}$
Rated angular velocity	ω_N [rad · s^{-1}]	300
Rated current	i_N [A]	5.8
Minimal moment of inertia	J_{min} [kgm^2]	$7.2 \cdot 10^{-3}$
Nominal moment of inertia	J_{nom} [kgm^2]	$17.7 \cdot 10^{-3}$
Maximal moment of inertia	J_{max} [kgm^2]	$31.3 \cdot 10^{-3}$
Viscous friction	B_m [Nms · rad^{-1}]	$1.4 \cdot 10^{-2}$
VSI gain	K_{pp}	100
Pole pair	p	3
Torque constant	K_t [Nm · A^{-1}]	1.14
Motor resistance	R_s [Ω]	1.05
Motor inductance	L_s [mH]	12.7
Current limit	i_{lim} [A]	±5
Velocity limit	ω_{lim} [rad · s^{-1}]	±50
Switching frequency	f_s [kHz]	10

Experimental tests were conducted for all control methods described in Section 2 using a variable-frequency sinusoidal excitation, commonly referred to as a sinusoidal sweep signal with an amplitude of 0.5 and frequency range of 2÷10 Hz. This approach enabled simultaneous evaluation of both the reference trajectory-tracking accuracy and the system's response to potential resonances. The experiments were performed for three different inertia values: J_{min}, J_{nom}, and J_{max}. The nominal inertia J_{nom} corresponds to the operating condition for which the control structures were originally tuned. The control schemes were also tuned using a variable-frequency sinusoidal excitation, but only for half of the drive operating frequency range. This limitation was introduced to reduce the influence of potential mechanical imperfections on the tuning and to ensure identical environmental conditions for all methods. Such an approach additionally enables assessment of the algorithm's robustness to practical mechanical phenomena, including backlash, resonances, and other environmental disturbances.

Analysing variable-frequency sinusoidal signals purely graphically is challenging. Therefore, during the experiments, the integral square error (ISE) and the robustness sensitivity index *S* (Tarczewski et al., 2022) were calculated and analysed. These indices are defined as follows:

$$ISE(t) = \int_0^{t_i} \left[\theta_{ref}(\tau) - \theta(\tau)\right]^2 d\tau \tag{28}$$

$$S_{ISE}^{J_m} = \frac{dISE}{dJ_m} \frac{J_{nom}}{ISE_{nom}} \tag{29}$$

where: t_i – the integration time dISE – difference in the ISE values for the modified and nominal moments of inertia, dJ_m – change in the moment of inertia.

In this study, both increased and decreased inertia conditions are analysed. For the first case, the following sensitivity coefficients, derived from Eq. (29), were defined: S_{ISEp}^{inc}, S_{ISEpfs}^{inc}, S_{ISEpls}^{inc}. For the second case, the following coefficients were introduced: S_{ISEp}^{dec}, S_{ISEpfs}^{dec}, and S_{ISEpls}^{dec}. The quantities ISE_p, ISE_{pfs}, and ISE_{pls} denote the ISE values calculated for the entire experiment, the first second, and the last second, respectively.

During the experimental tests, the current ripples Δi_q and speed ripple $\Delta\omega$ were measured. For this purpose, 20 ms segments of the signals were recorded during motor acceleration, and the difference between the maximum and minimum values within each segment was calculated. To ensure measurement consistency, the segments were selected only during periods of constant acceleration and excluded any reversal points. The resulting values were calculated for 10 such 20-ms segments and subsequently averaged.

Using data from Table 4 and information from Section 3.1, the coefficients α, β, and γ of the function $g(e)$ given by Eq. (11) can be determined. Based on the VSI gain, inductance, and sampling time, the maximum possible change in current between two consecutive samples is approximately 0.78 A. Therefore, the $g(e)$ function should pass through the points (0, 0), (0.2, 0.38), and (0.78, 100). The second point was determined experimentally to limit the system response to current variations caused by the cogging torque, which was measured at approximately 0.2 A. Based on these points, the following coefficients were ultimately obtained: $\alpha = 277.13$, $\beta = 11.71$, $\gamma = 0.78$.

4.2. Experimental results

Figure 4 presents the time responses of the PMSM servo-drive to a variable-frequency reference input, where $\theta_{diff}(t) = \theta_{ref}(t) - \theta(t)$. At first glance, no major differences are visible between the classic cascaded structure (b) and the architecture with the predictive current controller (a). However, a deeper analysis, focusing on the first second of the motion and the final stage of the experiment, reveals lower current and speed ripples, as well as higher reference-position tracking accuracy. These observations are further confirmed by quantitative metrics summarised in Table 5. Their analysis indicates that the accuracy improvement achieved by the hybrid CCS method does not span the entire frequency spectrum of the reference signal. Instead, it is observed at high frequencies. This allows the conclusion that predictive current control in a servo-drive extends the system bandwidth while maintaining high accuracy and low speed and current ripple at low reference signal frequencies and, consequently, at low machine operating speeds.

Figure 5 illustrates the results for an identical experimental scenario as in Figure 4, with the distinction that the tests evaluated the full FGM-MPPC (b) and the hybrid FGM-MPPC (a). Primarily, attention should be drawn to the resonance amplification occurring around the 5th second. In the case of the full CCS and hybrid CCS, this phenomenon did not occur. This behaviour can be attributed to the highly aggressive system tuning, which aims to minimise the cost function and prioritises accurate trajectory tracking at low speeds. For a detailed accuracy assessment, it is worth examining Table 5, which shows excellent precision of the predictive methods at low speeds but a degradation in performance at higher velocities. It turns out that the hybrid FGM-MPPC structure provides better mechanical resonance compensation. However, the trade-off for improved tracking accuracy in this architecture is an increase in i_q current ripples, as indicated by the values in Table 5. Notably, comparing the detailed views of Figures 4 and 5 reveals fundamentally different approaches to position-error compensation between the full CCS and hybrid CCS methods, and between the full and hybrid FGM-MPPC approaches. The predictive methods exhibit highly dynamic compensation characteristics, whereas the cascaded structures display smoother, more gradual behaviour. The above analysis indicates that mitigating resonance amplification within the predictive structure could increase tracking accuracy relative to both the full CCS and hybrid CCS methods across the drive's entire operating frequency spectrum.

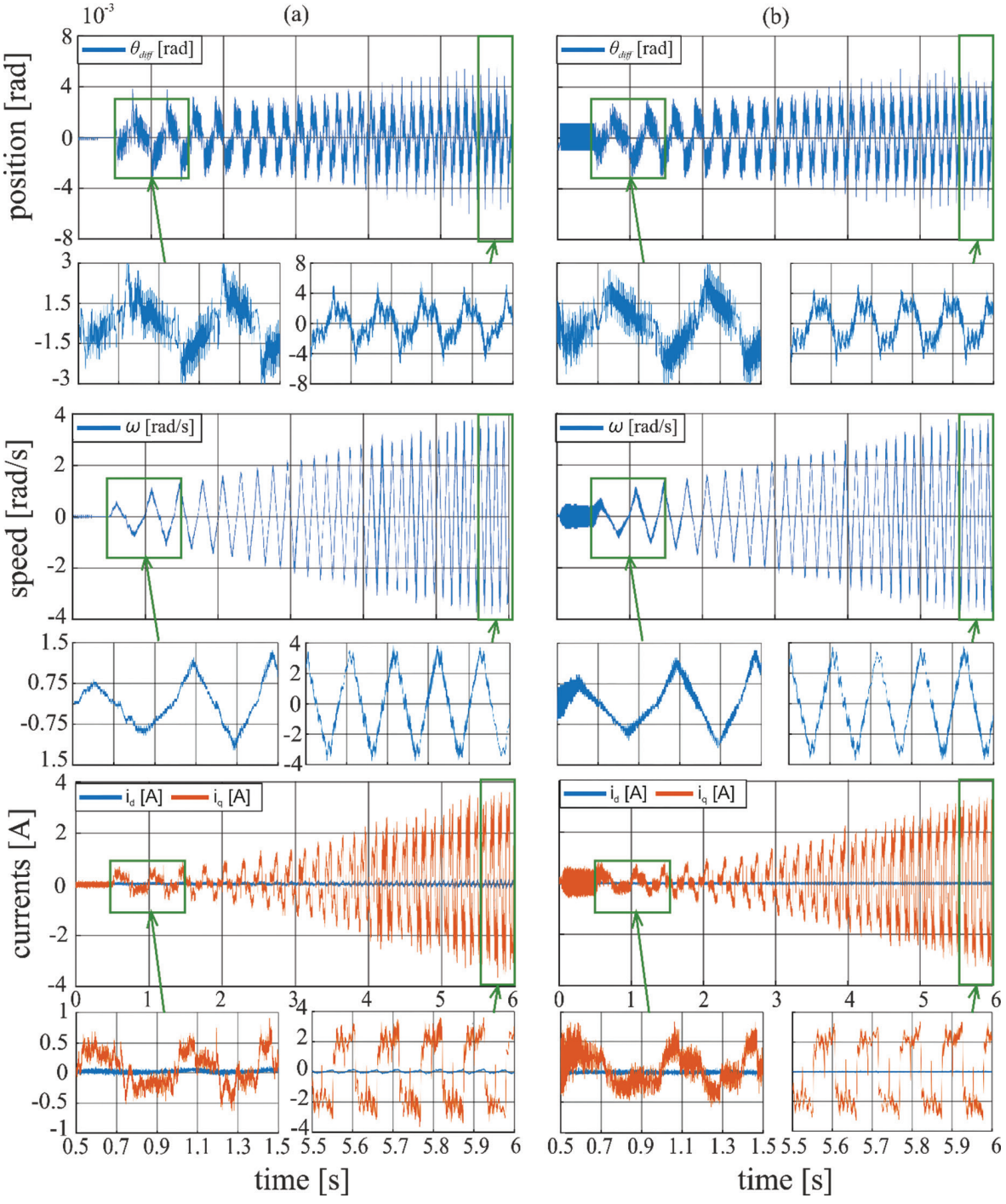


Figure 4. Experimental responses of PMSM servo-drive for variable frequency sinusoidal reference position: (a) – hybrid CCS, (b) – full CCS. CCS, cascaded control structure.

In addition to precise reference-position tracking, a key performance indicator of a servo-drive is its ability to perform load torque compensation. To evaluate this capability, experiments were conducted, and the results are shown in Figure 6. The results demonstrate that each evaluated control structure successfully compensates for the load torque under nominal inertia and is robust to variations in this parameter. The most effective disturbance rejection and compensation capabilities are demonstrated by the predictive methods (c) and (d).

Table 5. Performance indicator for variable frequency sinusoidal reference position.

Parameters	Full CCS	Hybrid CCS	Full FGM-MPPC	Hybrid FGM-MPPC
ISE_p [rad · s^{-2}]	$1.6373 \cdot 10^{-5}$	$1.3125 \cdot 10^{-5}$	$1.7955 \cdot 10^{-5}$	$1.0226 \cdot 10^{-5}$
ISE_{pfs} [rad · s^{-2}]	$0.1226 \cdot 10^{-5}$	$0.1266 \cdot 10^{-5}$	$0.0714 \cdot 10^{-5}$	$0.0661 \cdot 10^{-5}$
ISE_{pis} [rad · s^{-2}]	$0.4360 \cdot 10^{-5}$	$0.3328 \cdot 10^{-5}$	$1.0972 \cdot 10^{-5}$	$0.4819 \cdot 10^{-5}$
Δi_q [A]	0.6489	0.4387	0.6853	0.8403
$\Delta\omega$ [rad · s^{-1}]	0.3595	0.2996	0.3595	0.3596

CCS, cascaded control structure; FGM-MPPC, fast gradient method model predictive position control; ISE, integral square error.

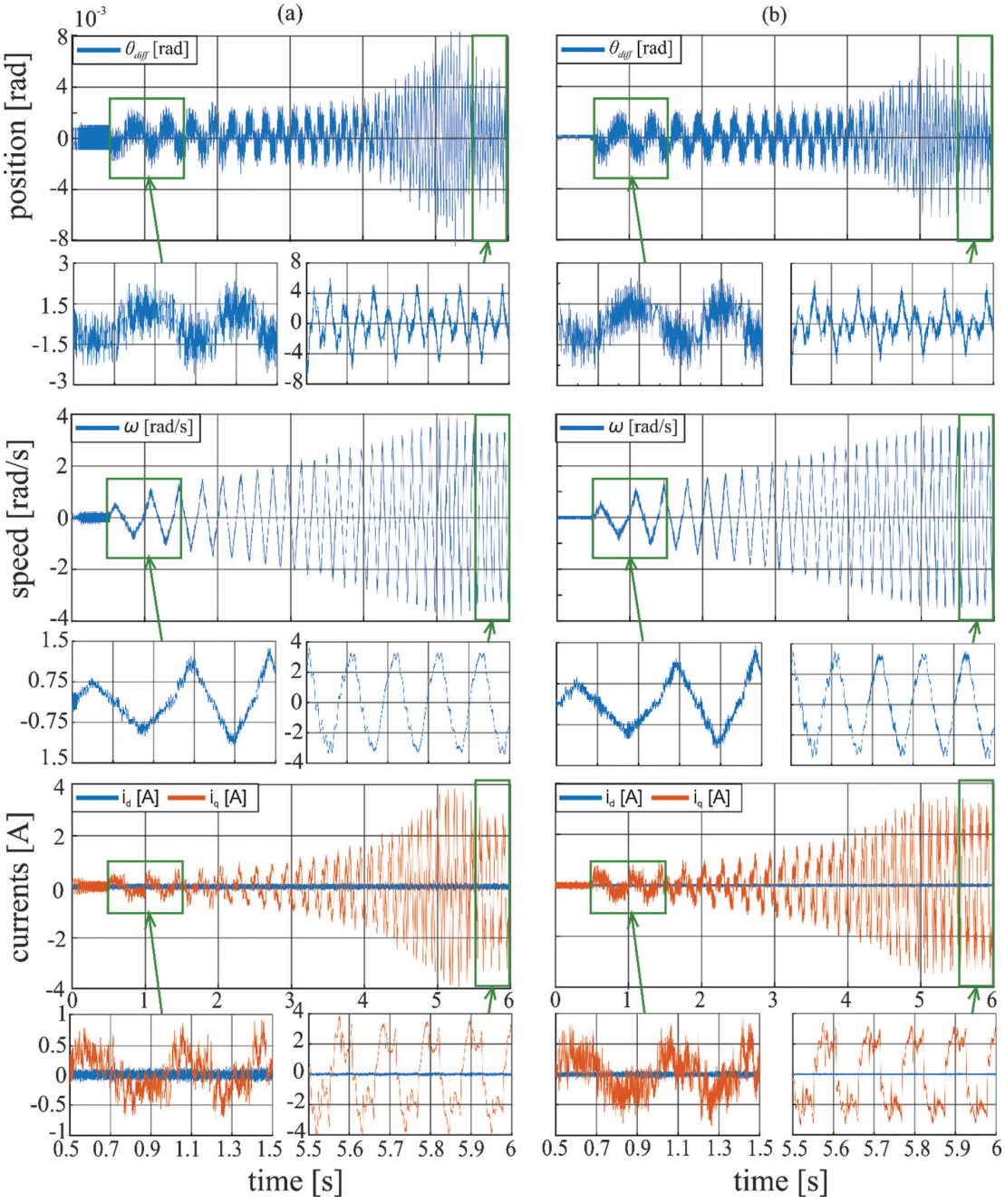


Figure 5. Experimental responses of PMSM servo-drive for variable frequency sinusoidal reference position: (a) – full FGM-MPPC, (b) – hybrid FGM-MPPC. FGM-MPPC, fast gradient method model predictive position control.

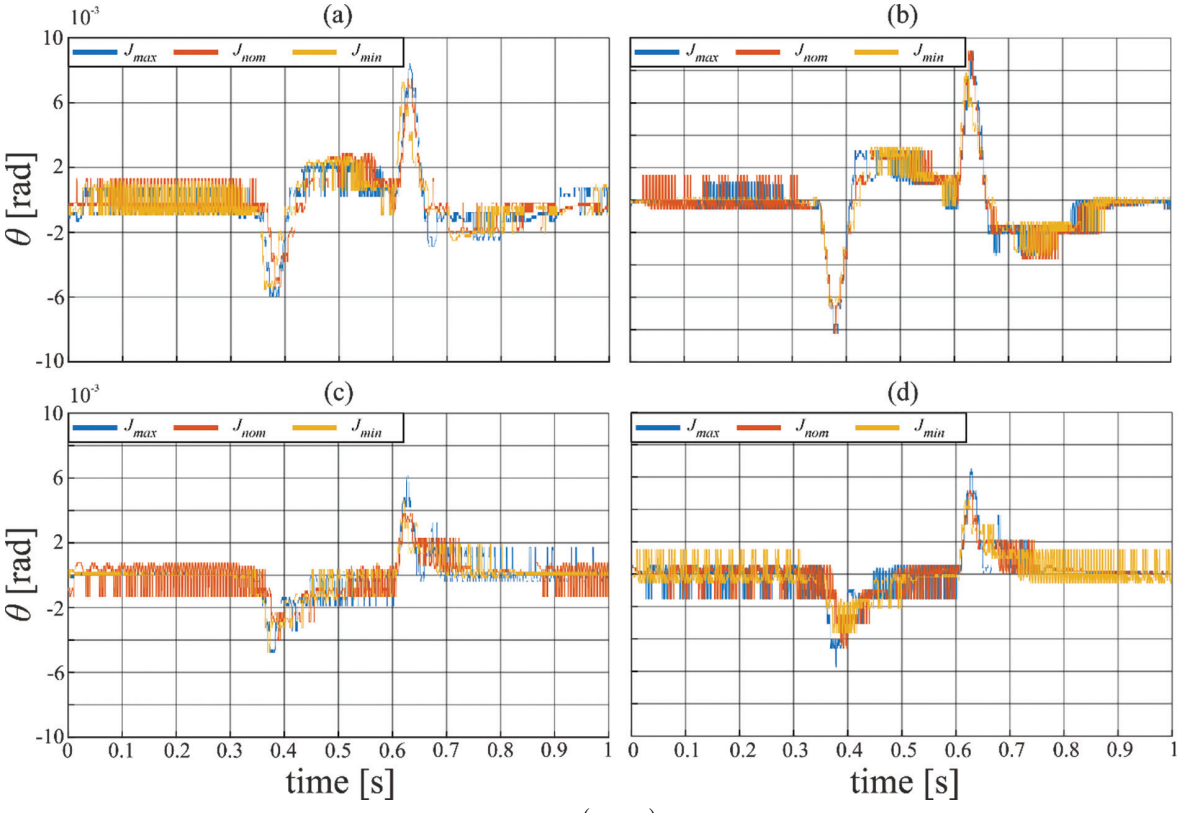


Figure 6. PMSM servo-drive responses during loading $T_L = 2\,Nm \in (0.3,\ 0.6)\,s$: (a) – hybrid CCS, (b) – full CCS, (c) – full FGM-MPPC, (d) – hybrid FGM-MPPC. CCS, cascaded control structure; FGM-MPPC, fast gradient method model predictive position control.

The next investigation focused on the robustness of the control structures to variations in the drive inertia. The results are presented in Figures 7 and 8. Figure 7 corresponds to the cascaded control methods, namely full CCS (b) and hybrid CCS (a), whereas Figure 8 presents the full FGM-MPPC approach (a) and the hybrid FGM-MPPC structure (b). The time-domain responses of the drive are complemented by the calculated sensitivity coefficients *S*, summarised in Table 6. Analysis of both the response plots and the sensitivity indices indicates that the predictive structures exhibit superior robustness, with the full FGM-MPPC method yielding the best results. The hybrid CCS demonstrates improved robustness across the drive's entire operating frequency range, as indicated by the $S_{ISEp}^{\ inc}$ and $S_{ISEp}^{\ dec}$ coefficients. However, an analysis of the sensitivity indices calculated for specific segments of the experiment, namely S_{ISEfs} and S_{ISEls}, reveals that the improvement in robustness is particularly pronounced at higher operating frequencies. In contrast, under low-acceleration, low-speed conditions, the robustness remains comparable to or slightly inferior to that of the reference methods.

5. Conclusions

In this paper, four different servo-drive control structures were implemented and experimentally evaluated with the objective of minimising trajectory tracking error while simultaneously ensuring high drive performance, namely low current and speed ripple, as well as robustness to variations in the moment of inertia. To this end, experimental investigations were conducted on a PMSM drive subjected to a variable-frequency sinusoidal excitation signal. The full and hybrid CCS structures were analytically tuned using the IMC and pole-placement methods, whereas the full and hybrid FGM-MPPC structures were tuned directly on the experimental setup using the ABC optimisation method.

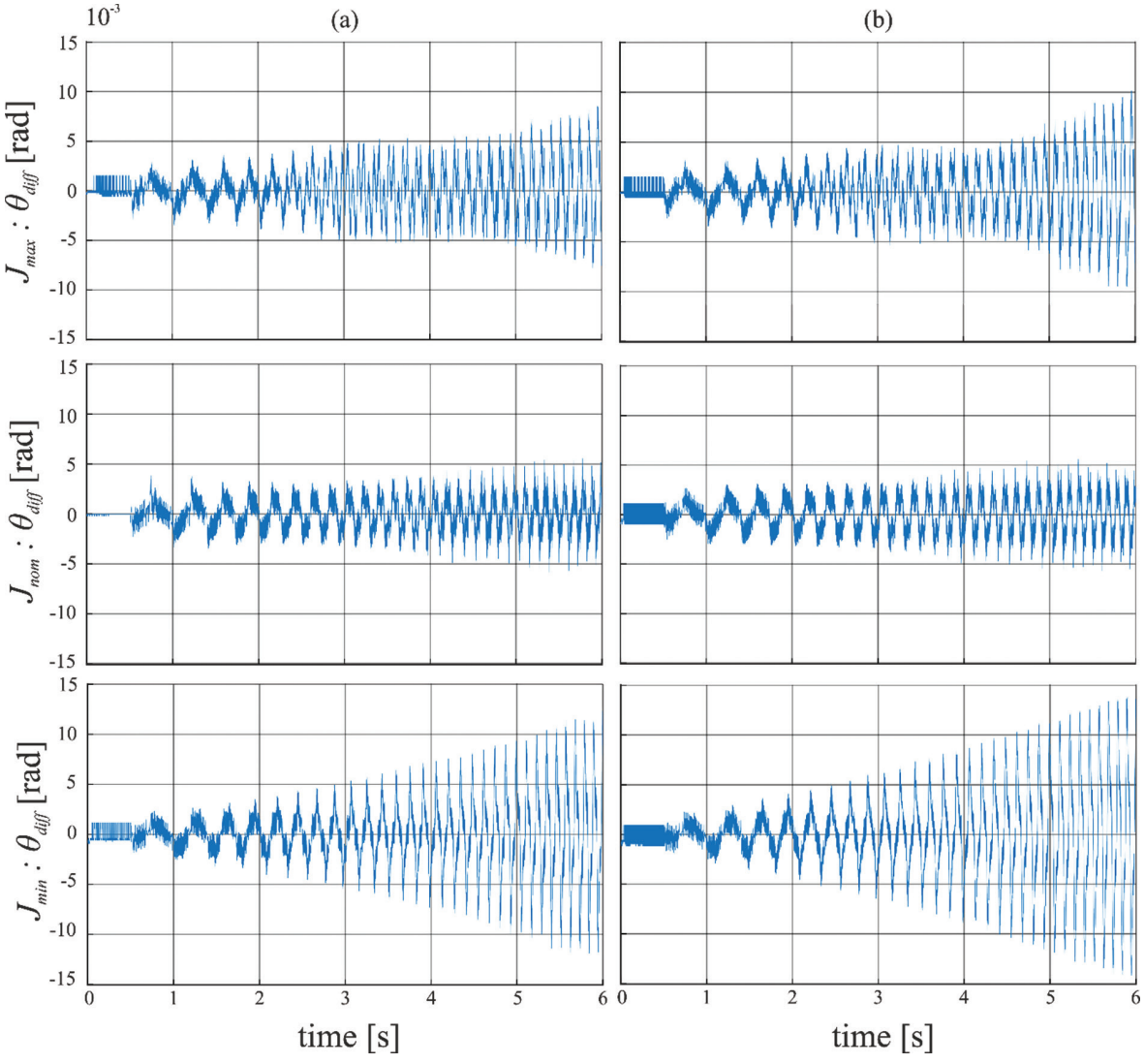


Figure 7. Experimental responses of PMSM servo-drive for variable frequency sinusoidal reference position with three different moments of inertia: (a) – hybrid CCS, (b) – full CCS. CCS, cascaded control structure.

The experimental results demonstrated that the hybrid CCS structure, compared with the full CCS, provides improved trajectory tracking accuracy, reduced current and speed ripples, and enhanced robustness to inertia variations. However, the hybrid FGM-MPPC approach achieved the highest tracking accuracy, but at the expense of increased current and speed ripple and reduced robustness compared with the proposed full FGM-MPPC controller. The study revealed that predictive control methods ensure very high trajectory tracking quality at low operating speeds. However, at higher speeds and during rapid position variations, these methods may become susceptible to resonant phenomena, limiting their practical applicability. This observation suggests that implementing effective resonance compensation could enable a fully predictive structure to achieve higher tracking accuracy and a wider bandwidth than cascaded and hybrid approaches, while simultaneously maintaining high robustness to inertia variations and low current and speed ripple at low operating speeds. Therefore, future work will focus on improving the fully predictive control structure in this field.

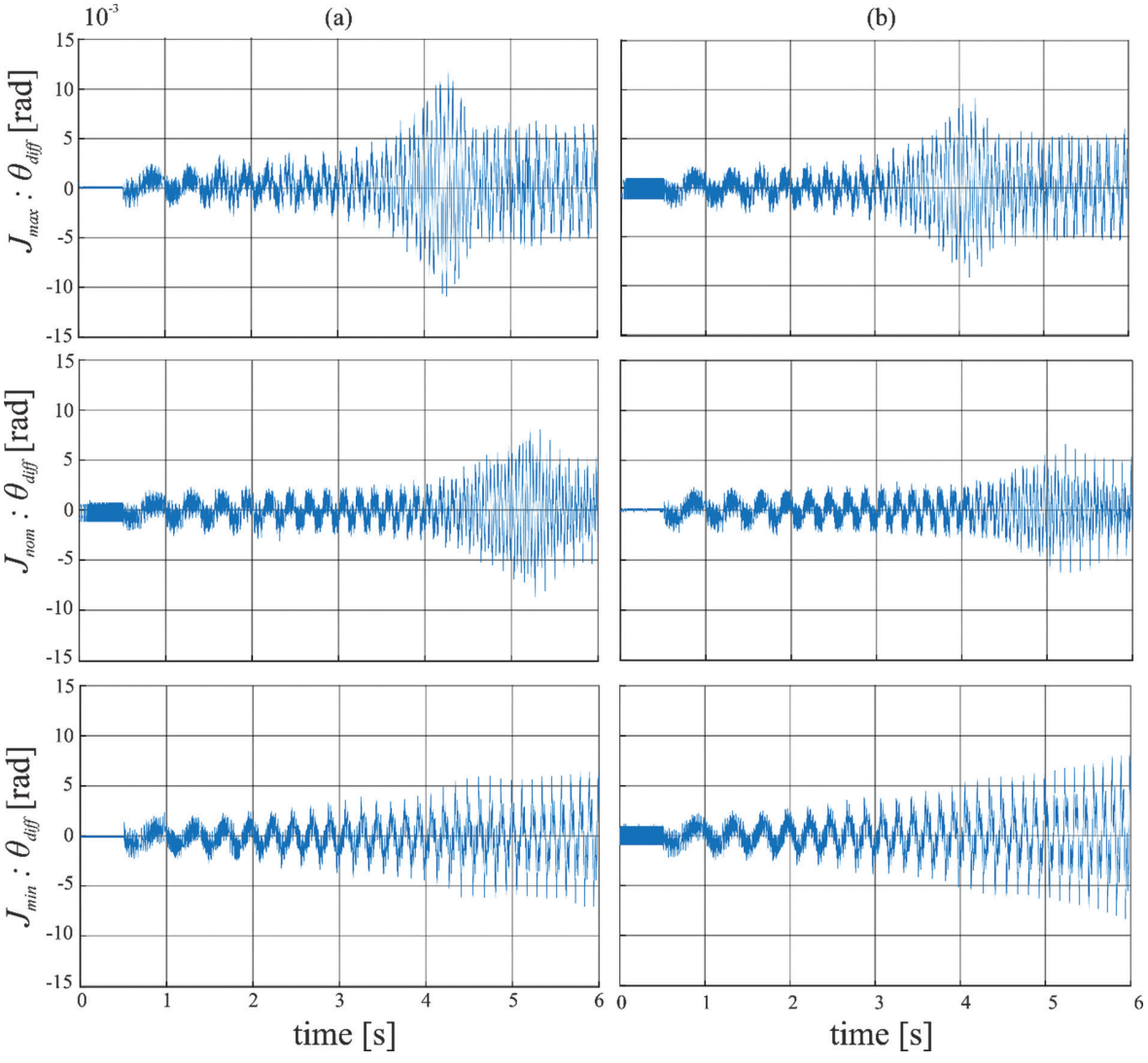


Figure 8. Experimental responses of PMSM servo-drive for variable frequency sinusoidal reference position with three different moments of inertia: (a) – full FGM-MPPC, (b) – hybrid FGM-MPPC. FGM-MPPC, fast gradient method model predictive position control.

Table 6. Sensitivity values.

Parameters	Full CCS	Hybrid CCS	Full FGM-MPPC	Hybrid FGM-MPPC
S_{ISEp}^{inc}	1.8169	1.7693	1.4862	2.2377
S_{ISEpfs}^{inc}	0.2643	0.4081	0.1445	−0.2517
S_{ISEpls}^{inc}	−12.8955	−9.1928	0.8108	1.0533
S_{ISEp}^{dec}	−3.4617	−2.3437	0.1143	2.2304
S_{ISEpfs}^{dec}	0.0813	−0.0861	0.0234	0.0590
S_{ISEpls}^{dec}	2.4444	2.1371	0.3077	0.3880

CCS, cascaded control structure; FGM-MPPC, fast gradient method model predictive position control.

References

Bahari, M., Mustalahti, P., Anaya, ÁP. and Matilla, J. (2026). Electrification of Heavy-Duty Robotic Manipulators via PMSM-Driven Electromechanical Linear Actuators. *IEEE Access*, 14, pp. 21805–21832. doi: 10.1109/ACCESS.2026.3662148

Bolun, W. Tao, Z. Zhengjin, S. and Hualiang, Z. (2022). Design of cascade model predictive controller for modular robot joints. *24th Chinese Control and Decision Conference CCDC*, 2022

Bożek, A. and Trybus, L. (2022). Tuning PID and PI-PI servo controllers by multiple pole placement. *Bulletin of the Polish Academy of Sciences: Technical Sciences*, 70(1), p. e139957. doi: 10.24425/bpasts.2021.139957

Brandstetter, P. and Krecek, T. (2012). Speed and Current Control of Permanent Magnet Synchronous Motor Drive Using IMC Controllers. *Advanced in Electrical and Computer Engineering*, 12(4), pp. 3–10. doi: 10.4316/aece.2012.04001

He, C., Hu, Ju, Ran, X., Wei, F., Li, Y. and Zhu, Y. (2024). A Simplified Constrained Predictive Position Control for PMSM Drives With Laguerre Functions. *IEEE Transactions on Industrial Electronics*, 71(12), pp. 15478–15487. doi: 10.1109/TIE.2024.3395753

Karamanakos, P., Liegmann, E., Geyer, T. and Kennel, R. (2020). Model Predictive Control of Power Electronic Systems: Methods, Results, and Challenges. *IEEE Open Journal of Industry Applications*, 1, pp. 95–114. doi: 10.1109/OJIA.2020.3020184

Kawai, H., Zhang, Z., Kennel, R. and Doki, S. (2023). Direct Speed Control Based on Finite Control Set Model Predictive Control With Voltage Smoother. *IEEE Transactions on Industrial Electronics*, 70(3), pp. 2363–2372. doi: 10.1109/TIE.2022.3174298

Li, S., Cai, M., Zhuo, L., Kennel, R., Heldwein, M. L. and Xu, Y. (2026). A Novel Constrained Offset-Free Model Predictive Position Controller for PMSM Drives With a Computationally Efficient Design. *IEEE Transactions on Power Electronics*, 41(2), pp. 1774–1787. Doi: 10.1109/TPEL.2025.3597678

Liu, S., Zhou, S., Abdullah, M., Liu, Z., Zhang, H. and Wang, R. (2026). Evaluation of servo fault and fault-tolerant control for heavy-legged robots under concurrent velocity sensor failures. *Control Engineering Practice*, 169, p. 106761. doi: 10.1016/j.conengprac.2026.106761

Mandra, S. (2014). Comparison of Automatically Tuned Cascade Control Systems of Servo-Drives for Numerically Controlled Machine Tools. *Elektronika ir Elektrotechnika*, 20(3), pp. 16–23. doi: 10.5755/j01.eee.20.3.2788

Richter, S., Jones, C. N. and Morari, M. (2012). Computational Complexity Certification for Real-Time MPC With Input Constraints Based on the Fast Gradient Method. *IEEE Transactions on Automatic Control*, 57(6), pp. 1391–1403. doi: 10.1109/TAC.2011.2176389

Richter, S. Mariéthoz and Morari, M. (2010). High-speed online MPC based on a fast gradient method applied to power converter control. *Proceedings of the 2010 American Control Conference,* Baltimore, USA, 2010

Rinaldini, M., Moslehi, M., Guglieri, G. and Primatesta, S. (2025). PID Tuning for PMSM-Quadrotor UAV System. *Engineering Proceedings*, 90(1), p. 2. doi: 10.3390/engproc2025090002

Sun, H. Chen, H. He, W. Zhang, G. Wu, L. and Zhang, Y. (2025). A Novel Model Predictive Controller Design for PMSM Drives in Electric Aircraft. *IEEE International Conference on Industrial Technology ICIT*, Wuhan, China 26-28 March 2025.

Sun, X., Lin, X., Han, S. and Wang, Y. (2025). An Improved Continuous-Control-Set Model Predictive Control for Dual Three-Phase PMSMs Based on Extended State Observer. *IEEE Transactions on Industrial Electronics*, 72(4), pp. 3449–3459. doi: 10.1109/TIE.2024.3454442

Tarczewski, T. and Grzesiak, L. M. (2016). Constrained State Feedback Speed Control of PMSM Based on Model Predictive Approach. *IEEE Transactions on Industrial Electronics*, 63(6), pp. 3867–3875. doi: 10.1109/TIE.2015.2497302

Tarczewski, T. and Grzesiak, L. M. (2018). An Application of Novel Nature-Inspired Optimization Algorithms to Auto-Tuning State Feedback Speed Controller for PMSM. *IEEE Transactions on Industry Applications*, 54(3), pp. 2913–2925. doi: 10.1109/TIA.2018.2805300

Tarczewski, T., Skiwski, M., Grzesiak, L. M. and Zieliński, M. (2018). PMSM Servo-Drive Fed by SiC MOSFETs Based VSI. *Power Electronics and Drives*, 3(1), pp. 35–45. doi: 10.2478/pead-2018-0001

Tarczewski, T., Szczepański, R., Erwiński, K., Hu, X. and Grzesiak, L. M. (2022). A Novel Sensitivity Analysis to Moment of Inertia and Load Variations for PMSM Drives. *IEEE Transactions on Power Electronics*, 37(11), pp. 13299–11330. doi: 10.1109/TPEL.2022.3188404

Wang, Y., Wu, Z. and Yu, G. (2025). Predictive Control of PMSM Based on a Fully Incremental Disturbance Model With Multiple Constraints. *IEEE Access*, 13, pp. 199036–199050. doi: 10.1109/ACCESS.2025.3635710

Xu, Z., Bu, F., Qin, H., Dong, Z., Guo, R., Du, R. and Deaconu, S. I. (2025). Control Performance Improvement of PMSM Direct-Drive Servo System at Low Speeds. *IEEE Journal of Emerging and Selected Topics in Power Electronics*, 13(2), pp. 1866–1878. doi: 10.1109/JESTPE.2025.3529851

Zhang, W., Zhang, Y., Liu, J., Liu, S., Xu, Y. and Zou, J. (2026). Model Predictive Direct Position Control Strategy Based on Point-to-Point Trajectory Planning for Fast Response of High-Inertia PMSM Servo System. *IEEE Journal of Emerging and Selected Topics in Power Electronics*, 14(2), pp. 2199–2210. doi: 10.1109/JESTPE.2025.3628939

Zheng, Y., Liu, M., Wu, H. and Wang, J. (2023). Analysis of Explicit Model Predictive Control for Track-Following Servo Control of Lunar Gravity Compensation Facility. *Applied Sciences*, 13(7), p. 4411. doi: 10.3390/app13074411

Zhuang, Y. Du, Q. Huang, W. Wang, Z. Wang, R. (2022). Model Predictive Current Control for PMSM Drives With Calculation Delay Compensation. *IEEE 5th International Electrical and Energy Conference CIEEC*, Nangjing, China, 27–29 May 2022.

Zuo, Q., Wang, B., Chen, J. and Dong, H. (2024). Model Predictive Control of Aero-Mechanical Actuators with Consideration of Gear Blacklash and Friction Compensation. *Electronics*, 13(20), p. 4021. doi: 10.3390/electronics13204021